Enhanced magnetic anisotropy in lanthanum M-type hexaferrites by quantum-confined charge transfer

Churna Bhandari, Michael E. Flatté, and Durga Paudyal

Phys. Rev. Materials **5**, 094415 — Published 30 September 2021

DOI: 10.1103/PhysRevMaterials.5.094415

Enhanced magnetic anisotropy in lanthanum M-type hexaferrites by quantum-confined charge transfer

Churna Bhandari,[1] Michael E. Flatté,[2,3] and Durga Paudyal[1,4]

[1] *The Ames Laboratory, U.S. Department of Energy, Iowa State University, Ames, IA 50011, USA*
[2] *Department of Physics and Astronomy, University of Iowa, Iowa City, IA 52242, USA*
[3] *Department of Applied Physics, Eindhoven University of Technology, Eindhoven, The Netherlands*
[4] *Departments of Electrical and Computer Engineering, and Computer Science, Iowa State University, Ames, Iowa 50011, USA*

Iron-based hexaferrites are critical-element-free permanent magnet components of magnetic devices. Of particular interest is electron-doped M-type hexaferrite i.e., $LaFe_{12}O_{19}$ (LaM) in which extra electrons introduced by lanthanum substitution of barium/strontium play a key role in uplifting the magnetocrystalline anisotropy. We investigate the electronic structure of lanthanum hexaferrite using a density functional theory with localized charge density which reproduces semiconducting behavior and identifies the origin of the very large magnetocrystalline anisotropy. Localized charge transfer from lanthanum to the iron at the crystal's $2a$ site produces a narrow $3d_{z^2}$ valence band strongly locking the magnetization along the c axis. The calculated uniaxial magnetic anisotropy energies from fully self-consistent calculations are nearly double the single-shot values, and agree well with available experiments. The chemical similarity of lanthanum to other rare earths suggests that LaM can host for other rare earths possessing non-trivial $4f$ electronic states for, *e.g.,* microwave-optical quantum transduction.

INTRODUCTION

Since the discovery of M-type hexaferrites in 1950, these complex oxides have been of continuing research interest for permanent magnets and magnetic memory devices[1–4], however the unique interplay between charge, spin, and orbital degrees of freedom suggest broader applications, including to quantum information science. M-type hexaferrites have a chemically and thermally stable crystal structure composed of easily accessible constituent elements in nature, especially barium hexaferrite and strontium hexaferrite.[2] The Gorter's type[5] hexaferrite has alternately aligned parallel and anti-parallel magnetic moments of ferric Fe^{3+} ions with respect to the hexagonal axis, aided by superexchange interaction via oxygen resulting in a large magnetic moment (20 μ_B per formula unit (f.u.)). The unique crystal structure leads to a huge uniaxial magnetocrystalline anisotropy (MCA) along the hexagonal axis, which assists their usage for high-frequency microwave elements (*i.e.* at low applied magnetic fields). An increase in the magnetic anisotropy constant (K_1) leads directly to higher-frequency microwave operation[6–8], assuming the microwave loss remains low.

A known approach to enhance the MCA is through replacement of the divalent barium with trivalent lanthanum in M-type hexaferrites[9–11]. The increase in the magnetic anisotropy was attributed to the extra electron added[9], with the suggestion that it leads to the formation of one Fe^{2+} per f.u. and thus enhances the orbital angular momentum. This is due to the extra occupancy of $3d$ state near the Fermi level specifically $3dz^2$ that leads to an additional contribution to the angular momentum as compared to Fe^{3+}. The increase of the orbital angular momentum provides, through the spin-orbit interaction (SOC), a stronger magnetic anisotropy.

Although the crystal structure consists of five Fe-sublattices at inequivalent crystal site locations (labelled 2a, 2b, 12k, $4f_1$, and $4f_2$), it is not clear where the added electron resides. Ref. 9 suggested the Fe (2a) site as a preferred site of electron localization, but there was no direct experimental measurement to confirm the formation of Fe^{2+}. Ref. 11 studied the charged states of Fe ions and inferred a partially quenched orbital moment of Fe (2a) from the anomalous behavior of the hyperfine field splitting in their Mössbauer spectroscopy measurement. A similar charge state is discussed in other Mössbauer experiments[12,13], but they did not conclusively determine the magnitude of orbital moment which is required to confirm the Fe^{2+} character.

Standard density functional theory (DFT) calculations predict a delocalized electronic state resulting from the additional electron introduced by the lanthanum[13], and thus predicts metallic behavior in disagreement with the experimentally observed semiconducting behavior. Thus it is not surprising that these calculations also yield an MCA much smaller than experimentally measured. In LaM, although Refs. 14 and 15 employed the same full-potential linearized augmented plane wave (FP-LAPW) methods, they obtained very different results, including for the spin magnetic moments of Fe. Ref. 15 could not conclusively find localization of extra electrons, which is expected in the delocalized electron state calculation. So, the discussion of MCA is irrelevant there. Ref. 14 found electrons localized at Fe (2a), however their calculated K_1 is smaller by a factor of two compared to the experiment for both SrM and LaM. A clear understanding of the proper electronic structure of lanthanum M-type hexaferrite (LaM) would thus provide a clear pathway towards describing the properties of $4f$-spin containing rare-earth-doped materials that are now used in other semiconducting rare-earth hosts like yttrium orthovana-

date and yttrium oxide.[16–18]

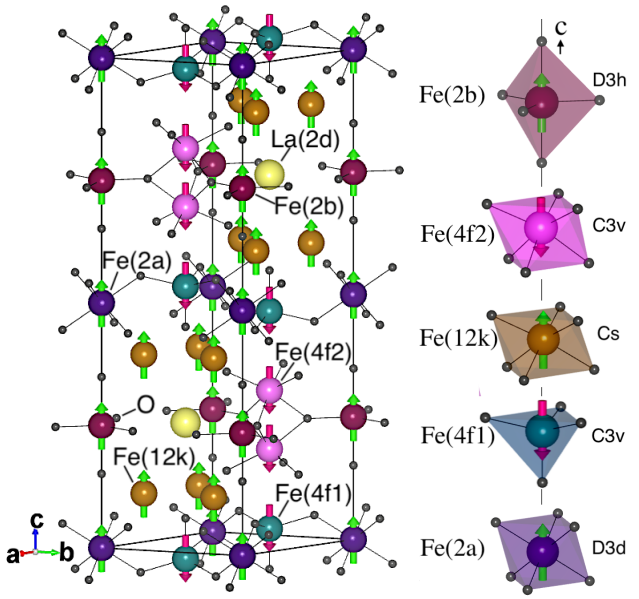

FIG. 1. (*Left*) Crystal structure of M-type hexaferrite ($LaFe_{12}O_{19}$) with Gorter's-type spin configurations of the different Fe sublattices. Violet, brown, and purple balls are Fe (2a), Fe (12k), and Fe (2b) with spin-↑(green) and dark green and magenta balls are Fe ($4f_1$) and Fe ($4f_2$) with spin-↓ (red), respectively. Yellow and black balls are La and O atoms. (*Right*) The polyhedra of each Fe-sublattice based on their nearest O atoms are shown with the site symmetries.

Here we investigate the electronic structure, optical behavior and magnetic properties of Ba/SrM and LaM using *localized* density functional theory (LDFT). The key results are: (i) replacement by La modifies the electronic band structure of BaM (SrM) significantly, producing a strongly localized band in the gap region, (ii) The electronic bandgap occurs between states of the same spin and is reduced, (iii) La-substituted electrons are strongly localized around the Fe (2a) site and occupy a localized ($3d_{z^2}$) band, (iv) The spin magnetic moment of Fe (2a) is reduced accordingly due to the formation of an Fe^{2+} charge state, and (v) The strongly localized extra electron enhances the K_1 by approximately two compared to BaM/SrM, which agrees with experiment.

METHODS AND CRYSTAL STRUCTURE

The first-principles calculations were performed by using the Vienna *ab-initio* Simulation Package (VASP) in the all-electron (AE) projector augmented wave (PAW) form[19,20] with the generalized gradient approximation (GGA) for the exchange-correlation functional including the Hubbard U corrections for Fe atoms. Following previous work[14], we used a Hubbard U_{eff} = 4.5 eV for Fe ($3d$) orbitals in our GGA + U calculations within Ref. 21's simplified rotationally invariant formalism in which only the effective value of $U_{eff} = U - J$ is relevant. We also performed the test calculations using rotationally invariant LSDA + U introduced by Liechtenstein *et al.*[22], but the results remain unchanged. We used a total energy plane wave cut off of 500 eV and $7 \times 7 \times 1$ **k**-mesh for the Brillouin zone sampling. In VASP, the spin-orbit coupling (SOC) correction can be obtained by fully relativistic noncollinear methods.[23] To compute the magnetic anisotropy, we used both single-shot and self-consistent schemes for the total energy calculations. For LaM, we did two set of DFT calculations: i) standard and ii) localized. In the localized DFT calculations a really high value of U_{eff} is used and it is subsequently reduced to a realistic value to avoid a higher-energy delocalized state solution. We first performed spin polarized DFT + U calculations and obtained delocalized solution (metallic state) for U_{eff} values up to 6 eV as also obtained in Ref.[15] In second set of calculations, we used a large value of $U_{eff} \sim 10$ eV, which gives a localized solution with emergence of a gap. Then we used the converged charge density obtained with the larger value of U_{eff} as a starting charge density and performed another set of fully self-consistent calculations with smaller values of $U_{eff} = 3 - 5$ eV. In later calculations, we always get finite gap for $U_{eff} \geq 3$, while its magnitude decreases with reducing value of U_{eff}. Then, we settled $U_{eff} = 4.5$ eV in the final calculations.

We used experimental lattice parameters measured by the x-ray diffraction method[13,24] in our calculations. We note that LaM undergoes a structural transition from hexagonal to orthorhombic at low temperature, but we neglect the low temperature structure in this work. The room temperature crystal structure has a hexagonal primitive unit cell with space group 194-P63/mmc (D^4_{6h}) as shown in Fig. 1, which consists of two formula units of $LaFe_{12}O_{19}$ and a total of 11 sublattices viz., five Fe at 2a, 2b, 12k and $4f_1$, $4f_2$, five O at $4f_1$, 4e, 12k, 12k, 6h, and 1 La at 2d Wyckoff positions. Fe (2a), Fe (12k), and Fe ($4f_2$) atoms form octahedral networks with O atoms with D_{3d}(-3m), C_s(m), and C_{3v}(3m) point group symmetry, while Fe ($4f_1$) forms tetrahedra with C_{3v}(3m) and Fe (2b) forms a bipyramidal structure with D_{3h}(-6m2) point group symmetry as shown in Fig. 1 (*Right*). We used the experimental structure parameters in our calculations to avoid the systematic lattice parameter overestimate from the GGA functional. We also did test calculations using the fully relaxed *ab initio* structure and found no significant changes in the properties.

RESULTS AND DISCUSSION

Evolution of electronic structure with La-substitution

We begin our discussion with the electronic band structure of the Gorter's type BaM ferrimagnet calculated along high symmetry **k** points as shown in Fig. 2. The

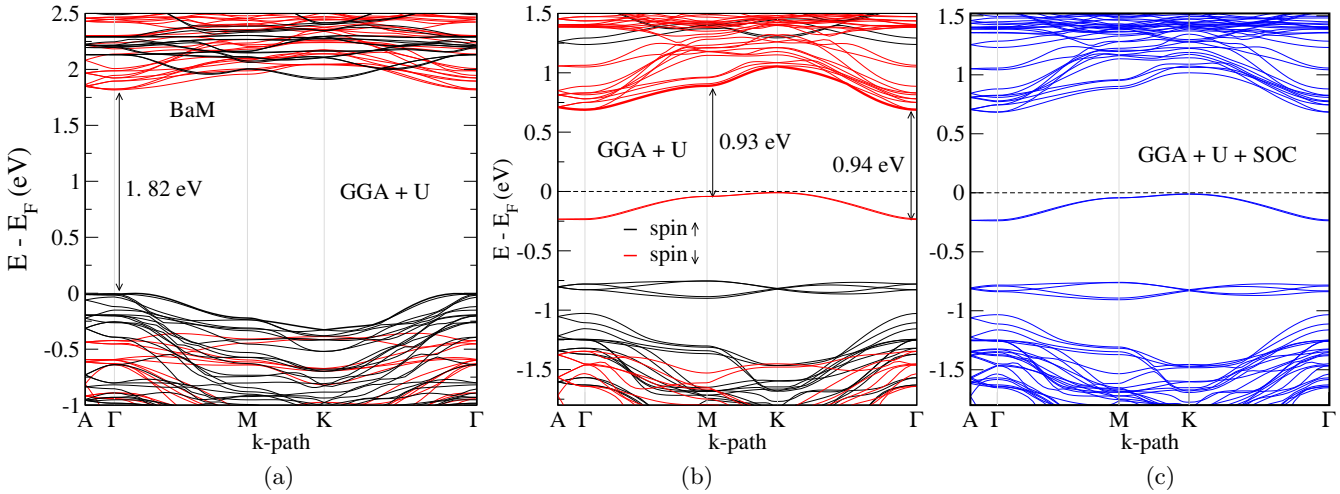

FIG. 2. Electronic band structure calculated using GGA + U of (a) BaM and (b) LaM and (c) GGA + U + SOC of LaM methods along high symmetry **k** points. The high symmetry points are: A $= \frac{1}{2}(0,0,1)$, Γ $= (0,0,0)$, M $= \frac{1}{2}(1,0,0)$, and K $= \frac{1}{3}(1,1,0)$ in units of primitive reciprocal lattice vectors, where $\vec{a} = a(1,0,0)$, $\vec{b} = a(-1/2, \sqrt{3}/2, 0)$, and $\vec{c} = (0,0,c)$ are primitive translation lattice vectors.

electronic band gap occurs between spin majority valence bands of Fe ($3d\uparrow$) and spin minority conduction bands of Fe ($3d\downarrow$). The valence bands consist of a strong admixture of Fe ($3d\uparrow$) with oxygen ($2p$), whereas conduction bands are mostly Fe ($3d\downarrow$). As is shown in Fig. 2(a), BaM has a direct band gap of 1.82 eV at Γ, computed with GGA + U methods, in good agreement with recent experiment[25] ($\sim 1.82 - 1.97$ eV). The lowest indirect band gap of 1.84 eV between the valence band maximum (VBM) (at A) and the conduction band minimum (CBM) (at Γ) is also not different from the direct gap as observed in the experiment. Although the experimentally observed indirect gap ($\sim 1.72 - 1.77$ eV) is slightly smaller than the direct gap, one cannot really distinguish them since they are very close. Also, the high symmetry **k**-point A is pretty much the same as Γ because the lattice constant c is much larger ($c \sim 4a$) as compared to a. We also computed the band structure of SrM (not shown here), which is very similar to that of BaM except in the magnitude of band gap. In order to correctly predict the band gap, a more advanced DFT functionals such as hybrid functional[26] and quasi-particle GW[27] approach are desirable, which is beyond the scope of this work.

The optical band gap related to the transitions between the valence and conduction bands with the same spins is larger by ~ 0.5 eV than the lowest direct gap. We found quite a bit increase of gap (2.34 eV) in the optimized structure, but the other properties such as magnetic moment and magnetic anisotropy constant remain the same as discussed elsewhere.[14] We also note that the magnitudes of calculated band gaps depend on the choice of Hubbard parameters, U and J. The sensible value of $U_{eff} = 4.5$ eV used in the calculations following the previous work[14] is based on its similarity to that obtained for Fe^{3+} in α-Fe_2O_3 with spectroscopic measurements[28] as well as for Fe^{2+} in FeO.[29]

Next, we discuss the electronic band structure of LaM. By performing the total energy calculations for different magnetic configurations, we confirmed that the Gorter's type of magnetic order is intact even with La-substitution. The ordinary DFT predicts a delocalized state of LaM leading to a half-metal (this band structure is shown in the Appendix Fig. 8). In contrast, experimentally LaM is a semiconductor.[10] The calculated electron from La-substitution is spread over all the Fe-sublattices, even though the occupancy is larger on Fe (2a) than the other iron sites. In essence, the small amount of the extra electron, when shared among the Fe sites, will not modify the Fe^{3+} charge state to Fe^{2+}. Indeed, the calculated values of the spin magnetic moments confirm these results, which are about the same ($4.10\mu_B$) for all Fe atoms as found in undoped BaM.

The true ground state is obtained by the localized DFT calculation which predicts correctly LaM as a semiconductor agreeing with the experiment. The calculated total energy per unit cell is also about 1 eV using $U_{eff} = 4.5$ eV in both calculations) smaller than that of the delocalized solution, confirming the global ground state property of the localized result. Since the delocalized solution is metastable, hereafter, we only discuss the results from the localized calculations.

Previous calculations in Ref. 14 and 15 did not study the band structure apart from structural change and charge state. In Ref. 15 authors calculated the density of states but it shows an incorrect metallic state. Therefore, to the best of our knowledge, the correct band structure of LaM has not yet been studied in the literature.

La substitution dramatically changes the band struc-

ture of BaM near the Fermi level. One can see the fully occupied two distinct subbands in the gap region in Fig. 2(b). The lower subbands consist of four and the upper subbands consist of a doubly degenerate band. A small indirect band gap of 0.77 eV opens up between the VBM at K and the CBM at Γ, which is about half of the BaM band gap. The reduction of the band gap is expected since the new bands show up in the middle of the gap.

Whereas our calculated band gap agrees with experimental measurements, its magnitude is larger than that obtained by the resistivity measurement (0.18 eV) in the ceramic LaM.[10] The band gap measured with this type of experiment would also be smaller for BaM (See the Ref. 10 for SrM). So, it would be interesting to see if one could perform a spectroscopic measurement of the gap in a LaM single crystal. The other interesting feature is the appearance of a pseudo-Dirac-like cone at the K-point in the lower subbands, which may lead to anomalous behavior in transport measurements in hole-doped LaM, which is worth future investigation. The GGA + U + SOC computed band structure in Fig. 2(c) does not show much difference compared to a calculation without SOC, except for a few split-off bands, which is expected because the SOC is weaker than the crystal field splittings in $3d$ elements.

Optical anisotropy

To further scrutinize the band gap, we computed the optical absorption coefficient (α) using GGA + U using the relation

$$\alpha(\omega) = \omega c^{-1} n(\omega)^{-1} \times \varepsilon_2(\omega), \tag{1}$$

where c is speed of light, ω is photon energy, $n(\omega) = \frac{1}{\sqrt{2}}[\varepsilon_1(\omega) + \sqrt{\varepsilon_1(\omega)^2 + \varepsilon_2(\omega)^2}]^{\frac{1}{2}}$ is refractive index, and $\varepsilon_1(\omega)$ and $\varepsilon_2(\omega)$ are real and imaginary parts of macroscopic dielectric constant. Neglecting the local field effects $\varepsilon_2(\omega)$ becomes:

$$\varepsilon_2(\omega) = \frac{4\pi^2 e^2}{m^2\omega^2} \sum_{v,c} \int_{BZ} \frac{d^3k}{(2\pi)^3} |\hat{e}\cdot\mathbf{M}_{cv}(\mathbf{k})|^2 \delta(\hbar\omega - \epsilon_{c\mathbf{k}} + \epsilon_{v\mathbf{k}}), \tag{2}$$

where $\hat{e}$ is the light polarization vector and $\mathbf{M}_{cv}(\mathbf{k}) = \langle\psi_{c\mathbf{k}}|\mathbf{p}|\psi_{v\mathbf{k}}\rangle$ is the momentum matrix element between the conduction and the valence states labelled by indices c and v respectively. The real part of the dielectric constant ($\varepsilon_1(\omega) \equiv \varepsilon(\omega)$) is obtained from $\varepsilon_2(\omega)$ using the Kramers-Kronig transformation:

$$\varepsilon_1(\omega) = 1 + \frac{2}{\pi}\mathcal{P}\int_0^\infty \frac{\omega' \varepsilon_2(\omega') d\omega'}{(\omega'^2 - \omega^2)}. \tag{3}$$

The results are shown in Fig. 3. We find α_{xx} for light polarization along $E \parallel a$ is stronger than α_{zz} for the light polarization $E \parallel c$ reflecting an anisotropy in the optical

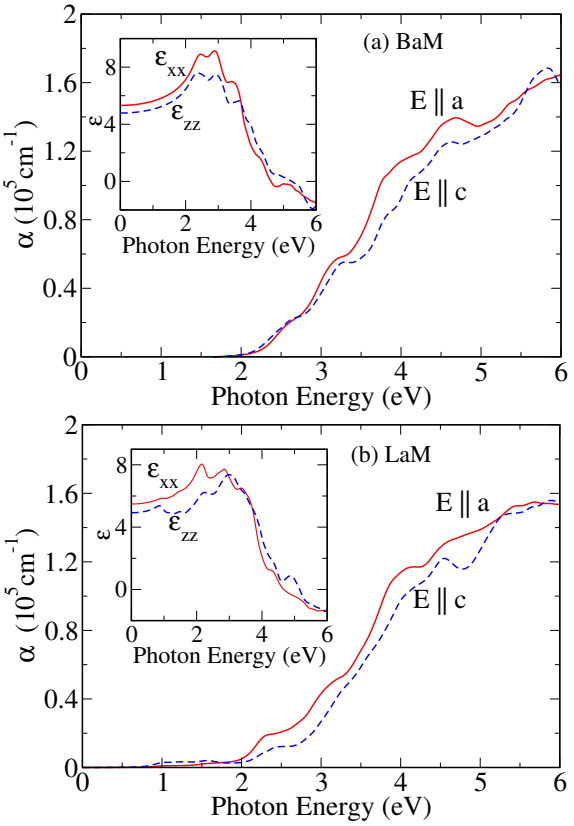

FIG. 3. Computed optical absorption coefficient ($\alpha(\omega)$) in units of cm^{-1} as a function of photon energy (in eV) for linearly polarized light in two different directions $E \parallel a$ and $E \parallel c$ using the GGA + U method in (a) BaM and (b) LaM. Inset figures show the real part of the dielectric constant ($\varepsilon_1(\omega) \equiv \varepsilon(\omega)$). The computed optical spectra show anisotropy between light polarization parallel to plane (ab) and perpendicular to plane (c) directions.

absorption in BaM. We note that x, y, and z correspond to the crystalline a, b, and c directions, respectively. The optical absorption is much weaker in the energy range (1.8 − 2.0 eV) which is expected since it corresponds to a $3d$-$3d$ transition. The optically disallowed transitions become allowed due to an admixture of Fe-$3d$ with $4s$ and $3p$ orbitals as is also seen in other $4d/5d$ oxides.[30,31] The real part of the dielectric constants $\varepsilon_{xx} = \varepsilon_{yy} = 5.32$ and $\varepsilon_{zz} = 4.79$ are consistent with the α, which also confirms the optical anisotropy.

In LaM, the optical absorption peak is red shifted by about 1 eV as expected due to the reduced band gap. The real part of the dielectric constants, $\varepsilon_{xx} = 5.5$ and $\varepsilon_{zz} = 4.95$, are similar to those in BaM. However the α in LaM shows a higher peak in the low energy region, differing that from BaM.

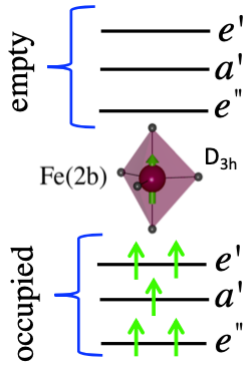

FIG. 4. Schematic diagram showing the crystal field splitting of single particle levels of Fe (2b) (FeO_5) with $3d^5$ valence electrons. Here $a^{'}$ and e are irreducible representations of the single particle $3d$ levels belonging to the D_{3h} point group of Fe (2b).

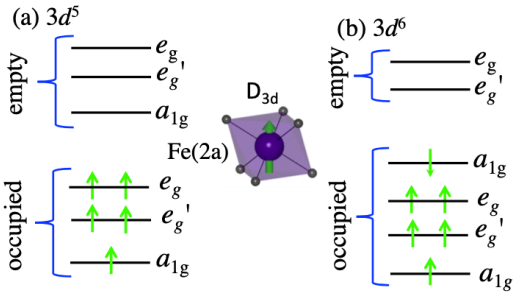

FIG. 5. Schematic diagrams showing the crystal field splitting of single particle levels for Fe (2a) (FeO_6 octahedra) with (a) $3d^5$ for BaM/SrM and (b) $3d^6$ valence electrons for LaM. Here a_{1g} and e_g are irreducible representations of the single particle $3d$ levels belonging to the D_{3d} point group of Fe (2a).

Quantum-confined charge transfer

There are five different Fe sublattices in LaM, but it is not clear which one is the most favorable for La-substituted electron localization. We address this issue by analyzing i) localized vs. delocalized solutions, ii) symmetry, and iii) partial density of states (PDOS). As described above, it is now clear that the delocalized solution is not correct as it predicts LaM is a metal. This has two main consequences: first, an electron cannot occupy the Fe atoms at 12k and $4f_1$ sites because one electron has to be shared among multiple Fe atom that are equivalent by symmetry. This scenario would lead LaM to be a metal. Second, if an electron would occupy the $4f_1$ or $4f_2$ sites, then it would further increase the net magnetic moment by 2 μ_B per cell, which is also not correct because the spin moments of Fe atoms at these sites are negative (anti-parallel to Fe at 2a, 2b, and 12k) and they would further decrease. This contradicts with the experimentally observed magnetic moment (38 μ_B per unit cell).

To gain a better insight into the electron localization, we employ the local symmetry of the Fe-O networks to analyze the single particle energy levels. According to C_{3v} site symmetry, the $3d$ orbitals of Fe tetrahedron at $4f_1$ site split into A_1, A_2, and doubly degenerate E irreducible representations. In the Fe ($4f_2$) the highly distorted octahedra with C_{3v} also lead to similar splittings of orbitals. The Fe (12k) octahedra has the lowest symmetry in which orbitals split into A and $A^{'}$ irreducible representations. In either case it is inappropriate for an electron to occupy any specific empty levels because of the continuum states present due to orbital overlaps between the nearest Fe atoms. Then we are left with the two sublattices at the 2a and 2b sites. In this case, one can anticipate a semiconducting state if one electron occupies either one of these two sites.

The local site symmetry of Fe (2b) is D_{3h} forming a bipyramidal (trigonal) FeO_5 unit. The Fe ($3d$) orbitals transform as $e^{''}(dyz, dzx)$, $a^{'}(d_{z^2})$, and $e^{'}(d_{xy}, d_{x^2-y^2})$ irreducible representations[32] as given in Fig. 4 for the ground state configuration $A_1^{'}$ with S=5/2 and L=0. The next electron would occupy the orbitally degenerate state $e^{''}$ which might lead to the well-known Jahn Teller distortion.[33] It is inappropriate for electron to occupy this site as it would cost extra energy.

On the other hand, the local site symmetry of Fe (2a) is D_{3d}, in which Fe (3d) orbitals transform as a_{1g}, $e_g^{''}$, and e_g irreducible representations. These two orbitally degenerate states with e_g irreducible representations are two dimensional and can mix with each other while a_{1g} cannot. Because of the trigonally distorted octahedral structure of Fe (2a), the ground state configuration consists of singly occupied five $3d$-orbitals in BaM and the corresponding levels are shown in Fig. 5(a). The lowest level is a d_{z^2} orbital which transforms as a_{1g}. irreducible representations with respect to the hexagonal axis indicating that any extra electron would occupy it (the opposite spin channel) first as shown in Fig. 5(b). We note that the symmetry of the single particle wavefunctions does not change due to the SOC, except the splitting of Fe (12k) into two sublattices.

To further confirm the electron localization as dictated by symmetry, we computed the PDOS for each atom with and without La substitution as shown in Fig. 6. As expected, the $5d$ states of La are located far above the Fermi level which is reflected in PDOS (shown in Appendix Fig. 9) indicating that it simply acts as an electron donor (similar to Ba except it donates an extra electron). Next, we discuss the PDOS of Fe atoms with and without La substitution. It is evident from Fig. 6(a) that the PDOS of all Fe atoms except Fe (2a) are unchanged with La substitution. No occupied states of Fe atoms are seen near the Fermi level except for Fe (2a). But the entire $3d$-band of Fe (2a) is shifted upwards showing a sharp peak below the Fermi level. To the best of our knowledge, this is the first prediction of such a quantum-confined charge transfer state in the La-substituted hexaferrites. Remarkably, it lies in the gap region and it is sharply localized at

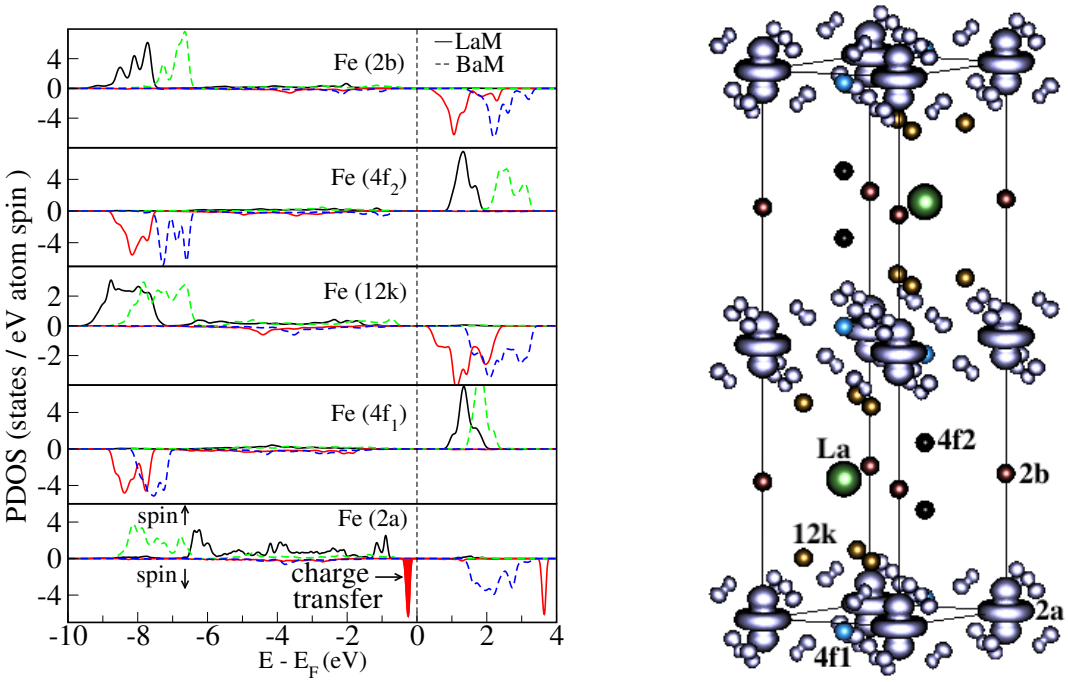

(a) (b)

FIG. 6. (a) Partial density of states (PDOS) of Fe atoms computed using GGA + U for BaM and LaM. The shaded red region below the Fermi level indicates the electron transfer to Fe (2a) from La. The solid (dashed) lines represent the PDOS in LaM(BaM) respectively. (b) Electron charge density contours computed in occupied region of valence bands (spin-down channel) with isosurface level 0.002 e/Å^3 in LaM, where Fe atoms are labeled according to their site symmetries. The contours further confirm that La-substituted extra electron charge is localized to Fe (2a) and nearby O atoms. The shape of contours around Fe atom is d_{z^2}-like and directed along the hexagonal axis.

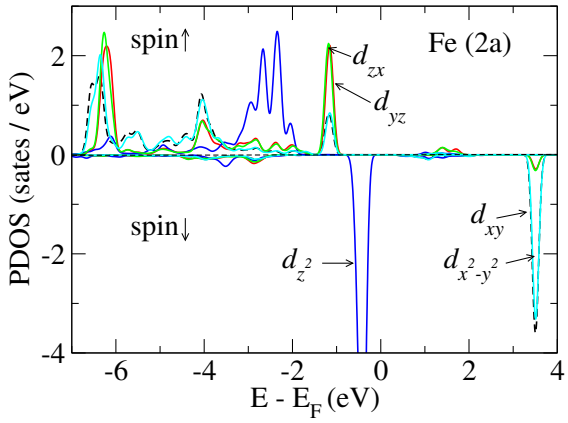

FIG. 7. Orbital resolved partial density of sates of Fe (2a) computed with GGA + U method in $LaFe_{12}O_{19}$. The sharply localized state below the Fermi level indicates the transfer of the La substituted electron into the d_{z^2}-derived orbital.

the Fe (2a) site consistent with the appearance of two narrow bands (each coming from one Fe (2a)). These results suggest that the La-substituted electron occupies a single orbital of the Fe (2a) site. As shown in Fig. 5, the transferred charge will occupy the a_{1g} (d_{z^2}) orbital which is parallel to the hexagonal axis (not the octahedral z-axis). To further confirm this, we computed the orbitally resolved partial density of states (Fig. 7), which shows that the band is derived from the d_{z^2} orbital of Fe (2a) consistent with the symmetry analysis. Electron charge distribution associated with this band is shown in Fig. 6 (b) by a charge density contour computed in the energy range from 0.5 eV below to the Fermi level. The contour shows a perfect d_{z^2} like shape pointing along the hexagonal axis at Fe (2a).

To quantify the charge localization, we computed the net charge transfer to each Fe atom by integrating the occupied region of the PDOS near the Fermi level as given in Table I. We find that 81% of the added electrons occupies Fe (2a), and the remaining amount is mostly shared between O and La atoms. This in turn suggests that the extra charge added to Fe (2a) would modify its Fe^{3+} charge state to Fe^{2+} consistent with the anomalous behavior of the hyperfine field splitting in Mössbauer spectroscopy.[12,13]

Magnetic moments and Curie temperature

The spin magnetic moments of individual atoms in BaM/SrM and LaM are given in Table II. The net magnetic moment of BaM/SrM is 39.98μ_B per unit cell which

TABLE I. Net amount of electron transfer to different Fe atoms in $LaFe_{12}O_{19}$. The tabulated values are per Fe atom and are expressed in units of electrons.

Atom	Fe (2a)	Fe (2a)	F e(12k)	F e($4f_1$)	Fe ($4f_2$)	La/O
electron	0.8127	0.0005	0.0038	0.0002	0.0065	0.1505

is consistent with the Gorter's type magnetic order as discussed above. The sum of the magnetic moments of the individual atoms is slightly smaller than the total value as expected since these are calculated within the atomic spheres, which exclude the interstitial contributions. Our calculated magnetic moments for individual Fe atoms are slightly larger than experimental values due to the following factors: (1) theoretical values depend on the choice of Hubbard parameters and the size of the atomic radii used in the calculations, (2) the experimental values measured at finite temperature are about 10% smaller than ideal values (5 μ_B) at zero K, and (3) there is a strong hybridization between Fe ($3d$) and O(p) orbitals. Indeed, some oxygens have magnetic moments up to 0.33 μ_B as given in Table II.

TABLE II. Spin magnetic moment of individual atoms in Sr/Ba/$LaFe_{12}O_{19}$ (Sr/Ba/LaM), the total magnetic moment per unit cell (which also includes the interstitial contribution), and comparison with experiment. Also shown are experimental magnetic moments (average values for LaM measured at room temperature).

Atom (site)	SrM This work	BaM This work	LaM This work	LaM Expt.
Fe (2a)	4.11	4.23	3.69	3.35
Fe (2b)	4.08	4.14	4.15	3.83
Fe (12k)	4.16	4.24	4.24	3.73
Fe (4f1)	-3.97	-4.12	-4.19	-3.83
Fe (4f2)	-4.11	-4.18	-4.11	-3.90
O (4e)	0.34	0.33	0.33	
O (4f)	0.09	0.08	0.11	
O (6h)	0.05	0.04	0.04	
O (12k)	0.17	0.17	0.12	
O (12k)	0.09	0.03	0.05	
Sr/La (2d)	0.00	0.00	-0.01	
Total	39.98	39.97	38.00	

All experiments see a smaller value for Fe (2a) than the other Fe sites. We again emphasize that the discrepancies between theoretical and experimental values appear to be similar for La substituted cases or not, as discussed above.

As the calculated spin magnetic moment suggests the formation of a Fe^{2+} state at the 2a site, the orbital magnetic moment is expected to belarger than in Fe^{3+} ($3d^5$, L=0) following the Hund's rule. However, its magnitude is much smaller ($\sim 0.1\mu_B$) than expected for Fe^{2+} ($3d^6$, L=2)[11] due to the partial quenching of the orbital moment by the crystal field. Indeed, the PDOS shows that, the extra charge occupies the d_{z^2} orbital with the z-component of angular momentum $L_z \sim 0$. Although the orbital moment is small, it is still increased by about 10% in LaM as compared to SrM for Fe (2a) and it qualitatively supports the hyperfine splitting data in which the Fe at 2a site shows a transformation from Fe^{3+} to Fe^{2+}.[11]

TABLE III. Calculated Curie temperature T_C and its comparison with previous theory and experiment for Sr/Ba/$LaFe_{12}O_{19}$ (Sr/Ba/LaM).

Methods	SrM	BaM	LaM
Expt.	737[36]	723	695
This work[a]	893	880	851
Theory[b]	-	1514	1419
Theory[c]	-	1009	946
Theory[d]	-	$\sim$ 1500	-
Theory[e]	-	$\sim$ 1000	-

[a] Hubbard, U_{eff}=4.5 eV
[b] Mean field approximation (MFA), U_{eff}=3.4 eV[34]
[c] Random phase approximation (RPA), U_{eff}=3.4 eV[34]
[d] MFA, U_{eff}=4 eV[35]
[e] RPA, U_{eff}=4 eV[35]

We now discuss the Curie temperature (T_C) and compare with previous results.[34,35] We consider an isotropic exchange interaction (J_{ij}) between the nearest neighbor Fe atoms within the mean field approximation. Although more involved approaches such as the random phase approximation (RPA) and mean-field approximation (MFA) have been employed previously[34,35] to estimate T_C, its magnitude is overestimated relative to experiments when reasonable values of the Hubbard U are used. Our straightforward calculations, taking the the total energy difference between ferrimagnetic and ferromagnetic configurations, show that the energy required to break a bond between the nearest neighbor Fe atoms is: J_{ij} = 12.32, 12.13, and 11.73 meV in SrM, BaM, and LaM, respectively. The total energy difference (also the energy required to break a bond) reduces with an increasing value of U thereby reducing the T_C. Remarkably, by using $T_C \sim S^2 J_{ij}/k_B$, with $S = 5/2$ for each Fe atom, we get 893, 880, and 851 K for respective compounds obtained by using a realistic value of U_{eff} = 4.5 eV; these agree very well with experimental values as shown in Table III. Although the magnitudes are slightly overestimated, the trend of the relative differences agrees with the experiments.

Magnetic anisotropy

The magnetic energy cost to rotate the spontaneous magnetization $M = M_s(\sin\theta\cos\phi\hat{x} + \sin\theta\sin\phi\hat{y} + \cos\theta\hat{z})$ with respect to the crystalline axis is the magnetic anisotropy energy (E_a). Here, θ and ϕ are magnetization angles and $\hat{x}$, $\hat{y}$, and $\hat{z}$ are unit vectors. Phenomenologically, the magnetic anisotropy energy density for a given

TABLE IV. Calculated magnetic anisotropy constant K_1 (in MJ/m^3) of Sr/Ba/$LaFe_{12}O_{19}$ (Sr/Ba/LaM) and its comparison with experiment and previous theory.

	SrM	BaM	LaM
This work[a]	0.18	0.18	0.32
This work[b]	0.34	0.33	0.66
Expt.[38,39]	0.35 − 0.36	0.32 − 0.33	0.5 − 0.8
Theory [c]	0.18		0.36

[a] Single-shot calculations
[b] Fully self-consistent calculations
[c] FLAPW methods with U_{eff}=4.5 eV[14]

magnet is given by $\frac{E_a}{V} = K_1 \sin^2\theta + K_2 \sin^4\theta + K_3 \sin^6\theta$, where K_i is the ith order magnetic anisotropy constant and V is the volume of the magnet.[37]

For hard magnets the lowest order magnetic anisotropy constant K_1 dominates and its magnitude depends on the single ion and the dipolar moment (pair contribution) interaction energies. The single ion energy depends on the strength of the spin-orbit coupling (λ) and crystal field (Δ) and is much larger than the pair contribution.[37] Ref. 32 also showed from a model based on quantum many-body wavefunctions that the leading contribution is from a single ion for Fe (2b). The zero-field splitting (uniaxial splitting) parameter $D \sim 2\text{cm}^{-1}$ is two orders of magnitude larger than the dipolar spin-spin contribution. Therefore, here, we focus only on the single ion contribution to K_1.

First we computed the total energy along the two different crystalline axes viz., E_{100} along the a and E_{001} along the c-axis respectively. Then, the magnetic anisotropy energy is obtained as: $E_a = E_{100} - E_{001}$. The computed values of $K_1 = E_a/V$ are positive in all cases (Table IV) suggesting magnetocrystalline anisotropy with an easy axis along the crystalline c-axis. The values outside (inside) the parentheses are obtained with and without full self-consistent total energy calculations using the GGA + U + SOC methods. The magnitudes of K_1 are sensitive to the methods and depend on whether it is a single shot or fully self-consistent calculation, despite λ's relative weakness for Fe ($3d$) atoms. For instance, the computed value of K_1 is 0.34 MJ/m^3 for BaM with the fully self-consistent calculations, twice the single-shot value of 0.18 MJ/m^3. In principle the self-consistent method is a better approach because the effect of SOC is included properly in the charge density and therefore it is expected to predict better results. Indeed, the value of K_1 obtained with the fully self-consistent calculations is in excellent agreement with the experimental value (0.35 MJ/m^3). Similar values are predicted for K_1 in SrM in excellent agreement with the experiment, which is expected since in both cases we have similar chemical and structural environments e.g., *sp*-electron elements (Sr or Ba).

Again, in LaM the self-consistent value of K_1 is enhanced by about a factor of two compared to the single-shot value, as was found for the parent compounds (Ba/SrM). The magnitude of K_1 is increased in LaM by a factor ~ 2 compared to Ba/SrM which is in very good agreement with experiment (0.5-0.8 MJ/m^3).[9] The increase in magnetic anisotropy can be understood in terms of charge transfer, spin, and orbital moment. As discussed above, the charge from La substitution occupies the d_{z^2} orbital of Fe (2a) resulting in the net charge polarization along the c-axis along with the formation of a Fe^{2+} charge state. Although the orbital moment is expected to be quenched for Fe^{2+}, effectively it is still increased by $\sim 10\%$ in LaM and leads to a significant single-ion contribution to K_1.[40] Interestingly, it is about three times larger along the c-axis than in the planar direction, which indicates that it would cost more magnetic energy to rotate strongly polarized charge away from the c-axis leading to the enhancement of K_1 in LaM. The enhancement of the uniaxial magnetic anisotropy is indeed related to this enhanced orbital moment of Fe (2a) in the uniaxial direction as compared to the planar direction in accordance with Bruno's anisotropic model.[41]

CONCLUSION

We used *ab-initio* calculations to study the evolution of the electronic band structure and optical spectra of the hexaferrites after chemical substitution of a divalent *sp*-element (Ba/Sr) with a trivalent $5d$-element (La). Our localized DFT calculations predict a very sharply localized band in the gap in LaM which is revealed by the electronic band structure and PDOS. The origin of this localized band is due to quantum-confined charge transfer from the substituted La to a specific site [Fe (2a)], occupying the symmetry-allowed $3d_{z^2}$-derived orbital. The reduced value of the spin magnetic moment of Fe (2a) is consistent with localization of the additional electron there, leading to the formation of a Fe^{2+} charge state at the 2a site. The increase in electronic charge, which leads to a reduction in the spin moment and an increase in the orbital moment of Fe (2a) driven by this La substitution, results in an increase of the magnetic anisotropy by a factor of two in LaM as compared to Sr/BaM and agrees very well with available experiment. Our study opens up the possibility of exploring rare-earth-based electron-substituted hexaferrites as quantum spin systems because of the formation of this spatially localized quantum state in the gap. It also provides the description of a potential host for other $4f$ elements that would provide sharp optical transitions within the optical gap of the host, with these rare earth elements substituting for the lanthanum.

ACKNOWLEDGMENTS

This work is supported by the Critical Materials Institute, an Energy Innovation Hub funded by the U.S.

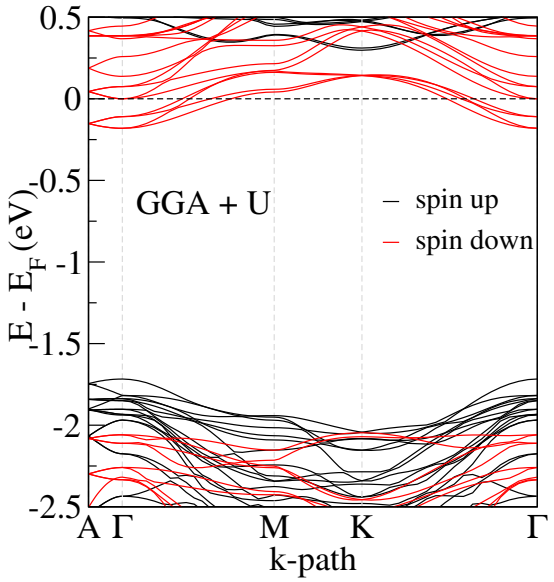

FIG. 8. Electronic band structure of metalstable ferrimagnet LaM calculated using the GGA + U method along high symmetry **k** points.

Department of Energy, Office of Energy Efficiency and Renewable Energy, Advanced Manufacturing Office. The Ames Laboratory is operated for the U.S. Department of Energy by Iowa State University of Science and Technology under Contract No. DE-AC02-07CH11358. MEF is supported by NSF DMR-1921877. We would like to thank C. Şahin for his useful remarks on the paper. We would also like to acknowledge Ed Moxley for maintaining and updating computational facilities and software.

Appendix A: Band structure of LaM with a delocalized electron

Here we present the band structure of the ferrimagnetic metallic metastable state of LaM shown in Fig. 8, computed using delocalized (standard) DFT. In this case, the electrons from La substitution partially occupy all the Fe sublattices, resulting in a half metal (as visible in the figure).

Appendix B: Density of states of LaM

We compare the PDOS of individual atoms in LaM in Fig. 9. The oxygen PDOS shows the average value of all oxygen atoms in unit cell as denoted by O (ave.). The La PDOS shows that 3*d* states are located farther away from the Fermi level, suggesting that it will donate an extra electron to the system. Indeed, the electron transfers to Fe (2a), because it has an extra localized band (with opposite spin) just below the Fermi level as discussed in the main text.

[1] K. Tsuyoshi, Annual Review of Condensed Matter Physics **3**, 93 (2012).
[2] J. M. D. Coey, IEEE Transactions on Magnetics **47**, 4671 (2011).
[3] R. C. Pullar, Progress in Materials Science **57**, 1191 (2012).
[4] "Global permanent magnets market share report, 2020-2027," .
[5] E. W. Gorter, Proceedings of the IEE - Part B: Radio and Electronic Engineering **104**, 255 (1957).
[6] H. Beljers, **9**, 131 (1954).
[7] C. Vittoria, Journal of Magnetism and Magnetic Materials **21**, 109 (1980).
[8] C. Patton, IEEE Transactions on Magnetics **24**, 2024 (1988).
[9] F. Lotgering, Journal of Physics and Chemistry of Solids **35**, 1633 (1974).
[10] M. Küpferling, P. Novák, K. Knìžek, M. W. Pieper, R. Grössinger, G. Wiesinger, and M. Reissner, Journal of Applied Physics **97**, 10F309 (2005).
[11] R. Grössinger, M. Küpferling, M. Haas, H. Müller, G. Wiesinger, and C. Ritter, Journal of Magnetism and Magnetic Materials **310**, 2587 (2007), proceedings of the 17th International Conference on Magnetism.
[12] D. Seifert, J. Tópfer, F. Langenhorst, J.-M. L. Breton, H. Chiron, and L. Lechevallier, Journal of Magnetism and Magnetic Materials **321**, 4045 (2009).
[13] M. Küpferling, R. Grössinger, M. W. Pieper, G. Wiesinger, H. Michor, C. Ritter, and F. Kubel, Phys. Rev. B **73**, 144408 (2006).
[14] V. c. v. Chlan, K. Kouřil, K. c. v. Uličná, H. Štěpánková, J. Töpfer, and D. Seifert, Phys. Rev. B **92**, 125125 (2015).
[15] P. Novák, K. Knížek, M. Küpferling, R. Grössinger, and M. W. Pieper, The European Physical Journal B - Condensed Matter and Complex Systems **43**, 509 (2005).
[16] J. M. Kindem, J. G. Bartholomew, P. J. T. Woodburn, T. Zhong, I. Craiciu, R. L. Cone, C. W. Thiel, and A. Faraon, Phys. Rev. B **98**, 024404 (2018).
[17] J. G. Bartholomew, J. Rochman, T. Xie, J. M. Kindem, A. Ruskuc, I. Craiciu, M. Lei, and A. Faraon, Nature Communications **11**, 3266 (2020).
[18] D. Serrano, C. Deshmukh, S. Liu, A. Tallaire, A. Ferrier, H. de Riedmatten, and P. Goldner, Phys. Rev. B **100**, 144304 (2019).
[19] G. Kresse and J. Hafner, Phys. Rev. B **47**, 558 (1993).
[20] G. Kresse and D. Joubert, Phys. Rev. B **59**, 1758 (1999).
[21] S. L. Dudarev, G. A. Botton, S. Y. Savrasov, C. J. Humphreys, and A. P. Sutton, Phys. Rev. B **57**, 1505 (1998).
[22] A. I. Liechtenstein, V. I. Anisimov, and J. Zaanen, Phys. Rev. B **52**, R5467 (1995).
[23] D. Hobbs, G. Kresse, and J. Hafner, Phys. Rev. B **62**, 11556 (2000).

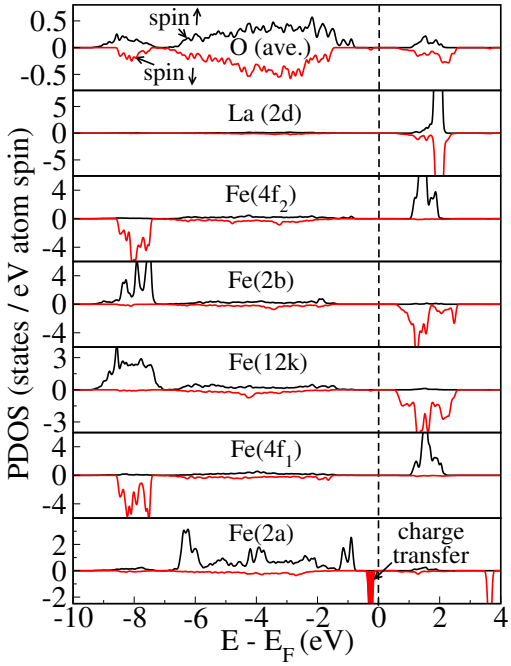

FIG. 9. PDOS of individual atoms in LaM where O (ave.) denotes the average PDOS of oxygens present in the unit cell.

[24] J. A. Kohn and D. W. Eckart, Journal of Applied Physics **35**, 968 (1964).

[25] A. Bañuelos-Frías, G. Martínez-Guajardo, L. Alvarado-Perea, L. Canizalez-Dávalos, F. Ruiz, and C. Valero-Luna, Materials Letters **252**, 239 (2019).

[26] J.-X. Shen, A. Schleife, A. Janotti, and C. G. Van de Walle, Phys. Rev. B **94**, 205203 (2016).

[27] L. Hedin, Phys. Rev. **139**, A796 (1965).

[28] R. Zimmermann, P. Steiner, R. Claessen, F. Reinert, S. Hüfner, P. Blaha, and P. Dufek, Journal of Physics: Condensed Matter **11**, 1657 (1999).

[29] M. Cococcioni and S. de Gironcoli, Phys. Rev. B **71**, 035105 (2005).

[30] C. Bhandari, Z. S. Popović, and S. Satpathy, New Journal of Physics **21**, 013036 (2019).

[31] C. Bhandari and S. Satpathy, Journal of Physics and Chemistry of Solids **128**, 265 (2019), spin-Orbit Coupled Materials.

[32] N. Fuchikami, Journal of the Physical Society of Japan **20**, 760 (1965).

[33] H. A. Jahn, E. Teller, and F. G. Donnan, Proceedings of the Royal Society of London. Series A - Mathematical and Physical Sciences **161**, 220 (1937).

[34] C. Wu, Z. Yu, K. Sun, J. Nie, R. Guo, H. Liu, X. Jiang, and Z. Lan, Scientific Reports **6**, 36200 (2016).

[35] P. Novák and J. Rusz, Phys. Rev. B **71**, 184433 (2005).

[36] Z. Zi, Y. Sun, X. Zhu, Z. Yang, J. dai, and W. Song, Journal of Magnetism and Magnetic Materials **320**, 2746 (2008).

[37] R. Skomski, *Simple Models of Magnetism* (Oxford University Press, Oxford University Press Inc., New York, 2008).

[38] L. Jahn and H. G. Müller, physica status solidi (b) **35**, 723 (1969).

[39] B. T. Shirk and W. R. Buessem, Journal of Applied Physics **40**, 1294 (1969).

[40] J. C. Slonczewski, Journal of Applied Physics **32**, S253 (1961), https://doi.org/10.1063/1.2000425.

[41] P. Bruno, Phys. Rev. B **39**, 865 (1989).